Exploring Frequency Band-Based Biomarkers of EEG Signals for Mild Cognitive Impairment Detection

Md. Nurul Ahad Tawhid, Siuly Siuly, *Member, IEEE*, Enamul Kabir, and Yan Li, *Senior Member, IEEE*

***Abstract*— Mild Cognitive Impairment (MCI) is often considered a precursor to Alzheimer's disease (AD), with a high likelihood of progression. Accurate and timely diagnosis of MCI is essential for halting the progression of AD and other forms of dementia. Electroencephalography (EEG) is the prevalent method for identifying MCI biomarkers. Frequency band-based EEG biomarkers are crucial for identifying MCI as they capture neuronal activities and connectivity patterns linked to cognitive functions. However, traditional approaches struggle to identify precise frequency band-based biomarkers for MCI diagnosis. To address this challenge, a novel framework has been developed for identifying important frequency sub-bands within EEG signals for MCI detection. In the proposed scheme, the signals are first denoised using a stationary wavelet transformation and segmented into small time frames. Then, four frequency sub-bands are extracted from each segment, and spectrogram images are generated for each sub-band as well as for the full filtered frequency band signal segments. This process produces five different sets of images for five separate frequency bands. Afterwards, a convolutional neural network is used individually on those image sets to perform the classification task. Finally, the obtained results for the tested four sub-bands are compared with the results obtained using the full bandwidth. Our proposed framework was tested on two MCI datasets, and the results indicate that the 16-32 Hz sub-band range has the greatest impact on MCI detection, followed by 4-8 Hz. Furthermore, our framework, utilizing the full frequency band, outperformed existing state-of-the-art methods, indicating its potential for developing diagnostic tools for MCI detection.**

Manuscript received 10 July 2023; revised 17 September 2023, 9 November 2023, and 14 December 2023; accepted 20 December 2023. Date of publication 25 December 2023; date of current version 16 January 2024. *(Corresponding author: Md. Nurul Ahad Tawhid.)*

Md. Nurul Ahad Tawhid is with the Institute for Sustainable Industries and Liveable Cities, Victoria University, Melbourne, VIC 3011, Australia, and also with the Institute of Information Technology, University of Dhaka, Dhaka 1000, Bangladesh (e-mail: md.tawhid1@live.vu.edu.au).

Siuly Siuly is with the Institute for Sustainable Industries and Liveable Cities, Victoria University, Melbourne, VIC 3011, Australia, and also with the Centre for Health Research, University of Southern Queensland, Toowoomba, QLD 4350, Australia (e-mail: siuly.siuly@vu.edu.au).

Enamul Kabir and Yan Li are with the School of Mathematics, Physics and Computing, University of Southern Queensland, Toowoomba, QLD 4350, Australia (e-mail: Enamul.Kabir@usq.edu.au; Yan.Li@usq.edu.au).

Digital Object Identifier 10.1109/TNSRE.2023.3347032

***Index Terms*— CNN, deep learning, electroencephalogram (EEG), frequency sub-band, mild cognitive impairment (MCI), spectrogram.**

I. Introduction

MILD cognitive impairment (MCI) represents a preclinical stage characterized by detectable cognitive impairment without reaching the level of overt dementia. MCI refers to a medical condition where there is a slight yet noticeable decline in cognitive functions, including memory, reasoning, and linguistic abilities [1]. MCI is considered an intermediate phase between the more pronounced cognitive decline observed in conditions like Alzheimer's disease (AD) and other forms of dementia and the normal cognitive changes associated with aging [2]. Neurocell death and dysfunction are the primary causes of this condition [3]. People with MCI have an increased risk of progressing to dementia, especially AD [4]. Dementia, a leading cause of disability among the elderly globally [5], is on the rise, particularly in emerging nations [2], [4], [5]. It is the seventh leading global cause of death and the second in Australia [6], [7]. Alarmingly, 75% of dementia cases worldwide go undiagnosed, with some nations reporting even higher rates [1]. The economic burden of dementia is substantial and projected to double by 2030, costing the US economy $1 trillion annually [1]. Since there is no cure for MCI, prevention is crucial for both economic and healthcare reasons. Early diagnosis and understanding its progression are essential to improve the quality of life for both MCI patients and their caregivers.

MCI research aims to discover cost-effective biomarkers with high sensitivity and specificity, although it is challenging due to symptom overlap with natural aging [8]. Several types of tests can be employed to explore MCI, including psychological assessments like the Mini-Mental State Examination (MMSE), blood tests, a computed tomography (CT) scan, spinal fluid analysis, neurological examinations, magnetic resonance imaging (MRI), positron emission tomography (PET), magnetoencephalography (MEG), and electroencephalography (EEG) [9], [10]. Among those techniques, MMSE is a manual question-and-answer test, and PET, MRI, and CT scans are expensive [1], [11]. In this study, we have used EEG data

for MCI detection as it is non-invasive, cost-effective, widely available, and portable [12], [13]. Moreover, it captures brain electrical activity over time, making it valuable for assessing cognitive concerns [3], [14], [15].

Recently, EEG-based biomarkers have become a useful tool in the study of MCI. Kashefpoor et al. [16] performed an EEG analysis employing simple spectral features using a Takagi-Sugeno neurofuzzy (NF) inference system with *k*-nearest neighbor (*k*NN). Khatun et al. [17] proposed a MCI detection method using single-channel EEG data. They extracted 590 features from the event-related potential (ERP) of the collected EEG signals, which included time and spectral domain characteristics of the response. Using support vector machine (SVM) method with a radial basis kernel (RBF), they achieved an accuracy of 87.9%. Yin et al. [18] extracted a set of features from resting-state EEG through spectral-temporal analysis and drove an optimal subset using a three-dimensional (3-D) evaluation algorithm. Using an SVM classifier, they achieved an accuracy of 96.94%. In [19], Sharma et al. used eight EEG biomarkers and obtained an accuracy range between 73.2% and 89.8%. Siuly et al. [1] utilized the piecewise aggregate approximation method to compress EEG data, employed permutation entropy and auto-regressive techniques to extract features, and applied the extreme learning machine (ELM) algorithm to achieve an accuracy of 98.78% for the classification of MCI subjects from healthy controls (HC) subjects. Alvi et al. [3] used a deep learning (DL)-based Gated Recurrent Unit (GRU) model for MCI detection from EEG data and obtained a classification rate of 96.91%. In another study [20], the same authors used another DL-based long-short-term memory (LSTM) model and produced 96.41% accuracy. Although several studies have aimed to classify MCI from HC subjects using EEG data, none have explored the important frequency sub-band in the EEG signal crucial for MCI detection, which is the main motivation of this study.

EEG signal has several rhythm bands like delta (0-4 Hz), theta (4-8 Hz), alpha (8-16 Hz), beta (16-32 Hz) and gamma (>32 Hz) [21]. Among those rhythm bands, <0.5 Hz and >32 Hz bands are considered noise [1], [18] and can be removed from the classification process. Studies like [1] and [18] have shown that the frequency band 0.5-32 Hz of EEG data is enough for classifying MCI from HC. But no prior research has investigated the most influential sub-band within those rhythmic bands for MCI detection. This study aims to fill that gap by identifying the crucial sub-band in EEG data for detecting MCI.

To address this gap, we have used the spectrogram image representation of the EEG signal for analysis purposes. An EEG spectrogram image shows the frequency composition of an EEG signal across time. In this two-dimensional graphic, the x-axis stands for time, the y-axis for frequency, and the color or intensity stands for the size or strength of the frequency components [9], [11]. Examining the spectrogram reveals variations in the frequency content of the EEG signal across time, showing patterns, oscillations, or events that may be useful for analysis or interpretation. Various studies have used time-frequency (T-F)-based images for the classification of neurological disorders such as epilepsy [22], epileptic seizures [23], clinical brain death diagnosis [24], schizophrenia [25], and autism spectrum disorder [9], [11] and obtained good classification performance. But to the best of our knowledge, no studies have used the spectrogram image-based EEG signal classification process for MCI detection. In this study, we have adopted this spectrogram image representation technique for EEG signals and used it to develop a framework to find out the important frequency rhythm in MCI detection.

In the proposed method, EEG data is first filtered using stationary wavelet transformation (SWT) and then segmented into small time frames. After that, we decomposed the filtered signal into four frequency sub-bands. Spectrogram images are generated for both the sub-bands and for the full filtered frequency band using the Short-Time Fourier Transform (STFT). Next, a DL-based convolutional neural network (CNN) is trained, and the classification process is carried out independently on the images for different sub-bands and on the full frequency band. Finally, the classification performance of the CNN model on different sub-band images is compared with the categorization performance using the full-band images to find out the important EEG rhythmic sub-band for MCI detection.

The major contributions of this study are as follows:

1) A noble framework is proposed to identify important frequency sub-bands of the EEG signal for MCI detection.
2) For the first time, an STFT-based spectrogram image with DL-based classification is used to detect MCI.
3) Explore the EEG signals' frequency bands that exhibit the highest responsiveness in identifying MCI.
4) Increase classification performance over existing approaches using the same dataset.

Paper organization: Section II discusses the proposed framework of this study. Results are described in Section III. Finally, Section IV gives the concluding remarks of this study.

II. Methods and Materials

In this research study, we have developed a spectrogram image-based important frequency band selection method for MCI detection from EEG signal data. Fig. 1 gives an overview of the proposed framework. A detailed discussion of the different steps involved in the proposed system is given in the subsections below.

A. EEG Data Collection

Here, we have used two publicly available EEG datasets of MCI. A brief description of those datasets is given below:

- The first dataset is collected from subjects admitted to the cardiac catheterization units of Sina and Nour Hospitals, Isfahan, Iran [16]. It contains EEG data from 27 subjects (11 MCI subjects with an age of 66.4 ± 4.6 and 16 HC subjects with an age of 65.3 ± 3.9) with elementary or higher education and a history of coronary angiography over the past year. Resting-state EEG data is recorded from 19 channels (Fp1, Fp2, F7, F3, Fz, F4, F8, T3, C3,

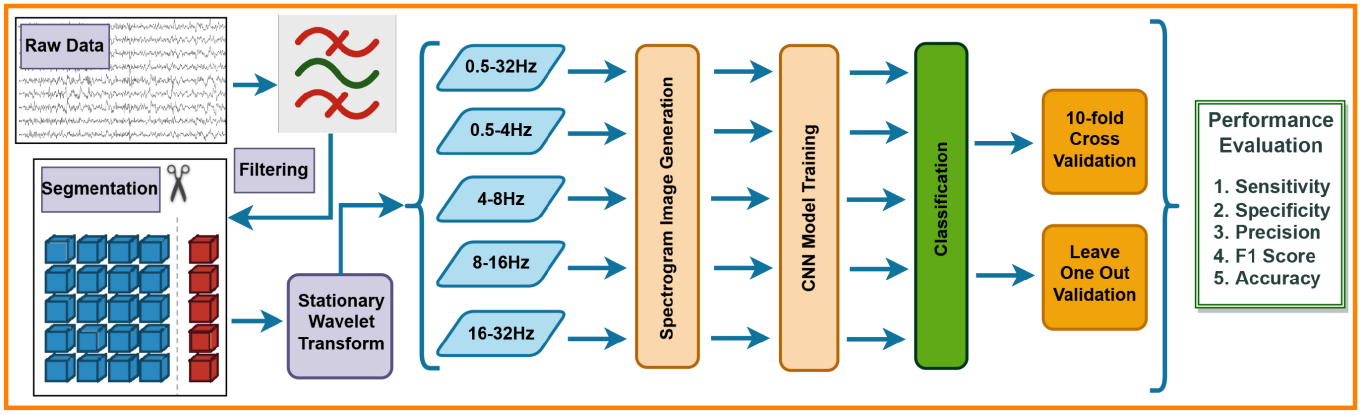

Fig. 1. Schematic illustration of the proposed framework and steps involved in the analysis.

Cz, C4, T4, T5, P3, Pz, P4, T6, O1, O2) according to the International 10-20 System at a sampling rate of 256 Hz.
- The second dataset consisted of 109 subjects (7 MCI patients with an age of 67 ± 7.6 and 102 HC subjects with an age of 72.2 ± 5.3) [26]. The signals are recorded in the resting state from 19 channels of a standard 10-20 EEG electrode system at sampling rates of either 128 Hz or 256 Hz. We have resampled all data to a common 256 Hz sampling frequency, a widely-used and computationally efficient choice for EEG data [27].

All of these datasets are freely accessible online, and each participant gave their informed consent to the release of their data at the time the data was collected. No ethical approval was needed for our study because we did not post any information that could be used to identify the respondents or compromise their confidentiality. Comprehensive explanations of these datasets have been left out due to space restrictions. References [16] and [26] contains more information on those datasets.

B. SWT Based Filtering of the EEG Signals

EEG signals may contain different kinds of noises, such as eye movements, ECG artifacts, pulse artifacts, respiration artifacts, skin artifacts, electrode artifacts, baseline drift, and power line interference. According to prior research [18], the most significant frequency bands of EEG signals are between 0.5 Hz and 32 Hz. Therefore, we have used SWT to filter the signals between 0.5 Hz and 32 Hz. SWT decomposes raw EEG signals into coefficients with various frequency ranges by using the appropriate decomposition level. In this study, we have used the decomposition level of 8, as shown in Fig. 2. After that, we removed the high (>32 Hz) and low (<0.5 Hz) coefficients as noise [18]. Finally, the denoised EEG signal is constructed from the remaining coefficients using the inverse stationery wavelet transformation (ISWT).

C. Segmentation of the EEG Signals

EEG recording is large-scale data, and processing this enormous dataset requires computational support and an expense of time [9], [11], [25]. Moreover, data scarcity is a major problem in the field of deep learning-based systems for EEG signal processing. Researchers typically utilize the segmentation strategy to tackle this issue. This technique divides the original EEG data into short, informative fragments and gives them the same level as the original signal, increasing the data sample size while preserving an equal ratio [9], [10], [11], [12], [13], [14], [25]. In this study, we have segmented the filtered signals into three-second (3s) time segments similar to the studies [12], [13], [14], as those studies have obtained better performance using 3s time segments that are computationally less expensive and also contain enough information to perform the automatic classification task [15].

D. Decomposition of the Signal Segments Into Different Frequency Sub-Bands

After segmentation of the signals, in this step, we have used SWT to decompose the signal segments into four frequency sub-bands: delta (0.5-4 Hz), theta (4-8 Hz), alpha (8-16 Hz) and beta (16-32 Hz) to check the important frequency band for MCI classification. In this classification process, we have tested all four of these frequency bands as well as the full frequency band of 0.5-32 Hz. Next, we will create spectrogram images using these signals across various frequency bands.

E. Spectrogram Image Generation

In this step, we have used the STFT-based plotting technique to generate the spectrogram images from the decomposed signal segments from the previous steps. Spectrogram is a popular technique for time-frequency domain analysis of EEG data that converts the time-varying EEG signal to a two-dimensional (2D) matrix with time and frequency axes [15]. In the spectrogram, time is usually displayed along the horizontal axis, with the duration of the EEG signal divided into segments or windows. The vertical axis represents the frequency range, typically from low frequencies (e.g., 0.5 Hz) at the bottom to higher frequencies (e.g., 32 Hz) at the top. In the spectrogram, color or intensity signifies the power or magnitude of the frequency component at each time and frequency point. Dark or low-intensity areas indicate lower power or the absence of frequency components, whereas

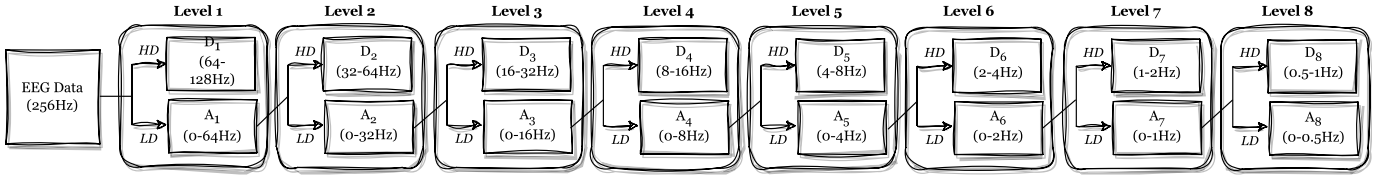

Fig. 2. SWT decomposition diagram of EEG signal for level 8.

brighter or higher-intensity areas denote higher power or the presence of frequency components [11].

Here, we have used the STFT-based plotting technique because it is widely used for generating spectrogram images from EEG data and has proven effective in classifying disorders like autism [9], [11], schizophrenia [25], and epilepsy [22]. Its simplicity of implementation and ability to provide a time-frequency representation of the data were key reasons for its integration into our framework. The calculation of the STFT involves dividing the signal into overlapping windowed blocks, and a hamming window is used to maintain continuity and avoid spectrum leakage [14]. The Fourier transform is then applied to each segment to derive its local frequency spectrum. The STFT of a signal at time t and frequency f, denoted as $STFT(t, f)$, can be calculated using the equation 1.

$$STFT(t, f) = \int_{-\infty}^{\infty} x(\tau) w(t-\tau) e^{-i2\pi f\tau} d\tau \qquad (1)$$

Here, $x(\tau)$ is the input signal, $w(t-\tau)$ is the window function at time t and $e^{-i2\pi f\tau}$ is the complex exponential term that performs the frequency analysis. STFT is frequently visualized by its spectrogram, which is an intensity representation of STFT magnitude over time. Here, we have generated the spectrogram plots for each of the signal segments for different frequency bands and saved those plots as images. These images are further used for feature extraction and classification in this study.

F. Proposed Model for Feature Extraction and Classification

In this study, we have used a DL-based CNN model to perform classification of the generated spectrogram images. CNN is a well-known DL-based image classification model that has demonstrated exceptional efficiency in classification by discovering appropriate features on its own and classifying data into several categories [28]. CNN model-based architectures have multiple convolution layers, which enables them to learn both low-level features like edges and textures and high-level features and semantic representations [28]. The learning of hierarchical representations helps the CNN comprehend complex visual patterns [11].

The convolution operation is a fundamental building block of CNNs and plays a crucial role in extracting and detecting meaningful features in images, enabling the network to perform tasks such as image classification, object detection, and more [39]. The internal operation of the convolutional layer with a spatial filter dimension of $M \times N$ and C number of channels can be expressed as follows:

$$Y_{i,j,k} = f\left(\sum_{m=1}^{M}\sum_{n=1}^{N}\sum_{c=1}^{C} W_{m,n,c,k} \cdot X_{i+m-1,j+n-1,c} + b_k\right) \qquad (2)$$

Here, $Y_{i,j,k}$ is the value at i^{th} row, j^{th} column, and k^{th} channel of the output feature map; $X_{i+m-1,j+n-1,c}$ is the value at the $(i+m-1)^{th}$ row, $(j+n-1)^{th}$ column, and c^{th} channel of the input feature map; $W_{m,n,c,k}$ is the weight of the m^{th} row, n^{th} column, c^{th} channel of the filter for the k^{th} channel of the output feature map; b_k is the bias term for the k^{th} channel of the output feature map; and $f(.)$ is the activation function applied to the element-wise sum. The equation computes the dot product between the filter weights W and the corresponding region of the input feature map X. The result is summed with the bias term b, and the activation function $f(.)$ is applied to introduce non-linearity.

To perform classification on the generated spectrogram images, we have used the third CNN model proposed and used by the authors of the study [11] for autism classification using spectrogram images. Although the authors of [11] presented three different CNN models, the third model performed the best in ASD classification, which is why we have used that model in this study. The model consists of four convolution (Conv) layers, three dropout layers, one fully connected layer, and a classification layer. Each Conv layer has a filter of 32 with a kernel size of 3×3 and is followed by a max pooling layer. The second and fourth Conv and Max pooling layer pairs are followed by a 25% dropout layer. The fully connected layer is followed by a 50% dropout layer. The final classification layer uses a softmax activation function to activate one of two outputs: HC or MCI. A categorical cross-entropy loss function and Adam optimizer are utilized to build the model. Table I lists the detailed configuration of those layers.

G. Performance Evaluation Techniques and Parameters

To assess our model's performance, we have employed two validation techniques: k-fold cross-validation (CV) and leave-one-out validation (LOOV). In k-fold CV, the data is divided into k equally-sized chunks. We have trained the model on k-1 of these chunks and validated it on the remaining one. This process repeats k times, ensuring that each chunk serves as a validation set exactly once. We then average the results across all iterations to evaluate the model's performance. We specifically used a 10-fold CV in this study.

In LOOV, we have excluded data from one subject during training, using the remaining subjects' data for model training. The omitted subject's data is subsequently used for validation. This process is repeated for each subject, and the final

TABLE I
ARCHITECTURE OF THE USED CNN MODEL

Layers	# Filter	Kernel size	Option
Conv2D	32	3×3	activation=relu
MaxPooling2D		2×2	
Conv2D	32	3×3	activation=relu
MaxPooling2D		2×2	
Dropout			25%
Conv2D	32	3×3	activation=relu
MaxPooling2D		2×2	
Conv2D	32	3×3	activation=relu
MaxPooling2D		2×2	
Dropout			25%
Flatten			
Dense	256		activation=relu
Dropout			50%
Dense (classifier)	2		
Total params: 1,209,058			
Trainable params: 1,209,058			

performance metrics are calculated over the full dataset by aggregating the results obtained from each iteration of LOOV.

Five well-known evaluation parameters are used to evaluate the performance of the proposed framework, namely: sensitivity (Sen), specificity (Spec), precision (Prec), F1 score (F1), and accuracy (Acc). We have also used the receiver operating characteristic (ROC) graph, a highly useful tool for visualizing the classifier's reliability, created by graphing sensitivity on the Y-axis and 1-specificity on the X-axis. A typical statistic for assessing the effectiveness of binary classifiers is the area under the ROC curve (AUC). The following inequalities are always maintained by the AUC value [11]:

$$0 \leq AUC \leq 1 \tag{3}$$

It is clear from equ. (3) that an AUC value of 1 indicates that the classifier has flawless discrimination abilities, whereas a value of less than or equal to 0.5 shows that the classifier has no discernment abilities at all [11]. These criteria allow us to grasp an idea about the classifier's behavior on the test data [1], [10], [12], [13], [14], [29], [30].

We have used the Gradient-weighted Class Activation Mapping (GRAD-CAM) visualization technique to interpret the decisions made by the proposed model [38]. Grad-CAM images display a color map on an input picture that indicates the significance of each region in the image in relation to the projected class. The colors in the picture that are close to red indicate that the area contains significant spatial characteristics for the projected class [38]. By visualizing which parts of an image are most influential in the classification decision, users can gain insights into model behavior and assess whether the model is making decisions based on relevant features [38].

III. RESULTS AND DISCUSSION

This section begins with a discussion of the experimental setup, followed by an in-depth presentation of the results. It concludes with a detailed analysis of the outcomes achieved.

A. Experimental Setup

As outlined in the methodology section, we have segmented the signals into 3s time frames, following a similar approach as in previous studies [9], [10], [11], [12], [13], [14], [25]. Subsequently, we have utilized STFT to generate spectrogram images from these signal segments. This process resulted in 6600 and 9600 images for MCI and HC subjects, respectively, in dataset 1. For dataset 2, these numbers were 924 and 2,536, respectively. In the case of dataset 2, we have created a balanced version by considering data from 33 subjects, resulting in 924 images for MCI subjects and 958 images for HC subjects. Each of these generated images is saved as a 224×224 pixel image to be used as input for the CNN model.

After image generation, the resulting datasets are used for both 10-fold CV and LOOV. The experiments are carried out on a computer with an AMD Threadripper Pro processor, 256 GB of RAM, and 48GB of graphics memory. We have used 50 epochs for training the model, as the model starts overfitting after those epochs. We have used mini-batch mode for batch size selection to speed up the learning process and tested three training batch sizes (32, 64, and 128) to train the model.

B. Results

In this study, we have developed a framework to identify important EEG signal frequency bands for MCI detection. We have extracted four frequency sub-bands (delta, theta, alpha, and beta) from the EEG signal (0.5-32 Hz), segmented the data into 3s time frames, and generated spectrogram images. We have compared these sub-band results with the full-band (0.5-32 Hz) results. We have employed both 10-fold CV and LOOV, testing three training batch sizes for the CNN model. Detailed experimental results for the proposed framework on three tested datasets are presented in Table II, including 10-fold and LOOV average performance values for various evaluation parameters across the three batch sizes.

From Table II, we can see that, for 10-fold CV in all the tested datasets, we have achieved the highest accuracy using the full (0.5-32 Hz) frequency band of the signal data. The highest accuracy we have obtained is 99.03% for dataset 1 and 100% for both the unbalanced and balanced versions of dataset 2. Now, among the tested sub-bands, for dataset 1, we have achieved the highest accuracy of 97.04% for the beta band, followed by 92.58% for the theta band. Alpha and delta have produced the third and fourth highest accuracy of 88.90% and 85.09%, respectively. For unbalanced dataset 2, we have observed similar results, with beta and theta bands producing 100% accuracy, followed by alpha and delta bands. For balanced dataset 2, we have achieved 100% accuracy for the beta, theta, and delta bands and 99.74% accuracy for the alpha band.

In terms of sensitivity, we have obtained the highest value of 99.12% using full band for dataset 1 and 100% for the other two datasets. Among the four sub-bands, beta has given 96.43%, theta 89.61%, alpha 85.16% and delta 81.77% for dataset 1. For the other two datasets, beta, theta, and delta have given 100% sensitivity, while alpha has given 99.82% and

TABLE II

10-FOLD AND LOOV AVERAGE PERFORMANCE VALUES WITH STANDARD DEVIATION (SD) OF DIFFERENT EVALUATION PARAMETERS FOR THE PROPOSED FRAMEWORK ON THE TESTED DATASETS WITH DIFFERENT TRAINING BATCH SIZES

		Dataset 1			Dataset 2 Unbalanced			Dataset 2 Balanced		
		32	64	128	32	64	128	32	64	128
Full (10-fold)	**Sen%**	**99.12±0.25**	98.87±0.44	98.95±0.55	**100.00±0.00**	**100.00±0.00**	98.95±0.55	**100.00±0.00**	**100.00±0.00**	**100.00±0.00**
	Spec%	98.91±0.41	**99.15±0.30**	99.07±0.21	**100.00±0.00**	**100.00±0.00**	99.07±0.21	**100.00±0.00**	**100.00±0.00**	**100.00±0.00**
	Prec%	98.42±0.59	**98.75±0.47**	98.66±0.30	**100.00±0.00**	**100.00±0.00**	98.66±0.30	**100.00±0.00**	**100.00±0.00**	**100.00±0.00**
	F1	**0.99±0.00**	**0.99±0.00**	**0.99±0.00**	**1.00±0.00**	**1.00±0.00**	0.99±0.00	**1.00±0.00**	**1.00±0.00**	**1.00±0.00**
	Acc%	98.99±0.24	**99.03±0.32**	99.03±0.29	**100.00±0.00**	**100.00±0.00**	99.03±0.29	**100.00±0.00**	**100.00±0.00**	**100.00±0.00**
Delta (10-fold)	**Sen%**	79.24±3.69	79.49±3.74	**81.77±2.39**	**100.00±0.00**	**100.00±0.00**	**100.00±0.00**	**100.00±0.00**	**100.00±0.00**	**100.00±0.00**
	Spec%	87.65±2.28	**88.27±1.71**	87.38±0.76	99.92±0.17	**99.96±0.12**	**99.96±0.12**	99.89±0.35	**100.00±0.00**	99.89±0.35
	Prec%	81.57±2.73	**82.35±1.99**	81.66±1.08	99.78±0.48	**99.87±0.41**	**99.87±0.41**	99.90±0.32	**100.00±0.00**	99.90±0.32
	F1	0.81±0.02	0.81±0.02	**0.82±0.01**	1.00±0.00	**1.00±0.00**	**1.00±0.00**	1.00±0.00	**1.00±0.00**	1.00±0.00
	Acc%	84.22±1.36	84.72±1.34	**85.09±0.95**	99.94±0.12	**99.97±0.09**	**99.97±0.09**	99.95±0.17	**100.00±0.00**	99.95±0.17
Theta (10-fold)	**Sen%**	87.86±2.23	89.46±2.75	**89.61±2.70**	**100.00±0.00**	**100.00±0.00**	**100.00±0.00**	99.90±0.33	**100.00±0.00**	99.90±0.33
	Spec%	93.24±1.70	93.10±1.76	**94.65±1.12**	**100.00±0.00**	**100.00±0.00**	99.96±0.12	**100.00±0.00**	**100.00±0.00**	99.89±0.34
	Prec%	89.98±2.20	90.01±2.02	**92.02±1.59**	**100.00±0.00**	**100.00±0.00**	99.87±0.41	**100.00±0.00**	**100.00±0.00**	99.90±0.32
	F1	0.89±0.02	0.90±0.02	**0.91±0.02**	**1.00±0.00**	**1.00±0.00**	1.00±0.00	**1.00±0.00**	**1.00±0.00**	**1.00±0.00**
	Acc%	91.06±1.37	91.63±1.52	**92.58±1.13**	**100.00±0.00**	**100.00±0.00**	99.97±0.09	99.95±0.17	**100.00±0.00**	99.89±0.22
Alpha (10-fold)	**Sen%**	84.87±1.51	84.46±2.47	**85.16±1.54**	99.68±0.68	**99.82±0.59**	99.67±0.54	99.57±0.76	**99.90±0.32**	99.68±0.52
	Spec%	91.42±2.00	**91.96±1.01**	90.77±1.53	99.92±0.16	99.84±0.29	**99.96±0.13**	99.56±0.57	99.58±0.71	**99.67±0.75**
	Prec%	87.26±2.28	**87.76±1.68**	86.45±1.63	99.76±0.51	99.59±0.69	**99.91±0.29**	99.59±0.52	99.57±0.76	**99.70±0.68**
	F1	**0.86±0.01**	0.86±0.02	**0.86±0.01**	**1.00±0.00**	**1.00±0.00**	**1.00±0.00**	**1.00±0.00**	**1.00±0.00**	**1.00±0.00**
	Acc%	88.75±1.12	**88.90±1.28**	88.49±0.69	99.86±0.25	99.83±0.36	**99.88±0.20**	99.58±0.48	**99.74±0.45**	99.68±0.51
Beta (10-fold)	**Sen%**	94.39±0.95	95.88±0.96	**96.43±0.78**	**100.00±0.00**	**100.00±0.00**	**100.00±0.00**	**100.00±0.00**	**100.00±0.00**	**100.00±0.00**
	Spec%	97.42±0.74	**97.68±0.47**	97.46±0.45	**100.00±0.00**	**100.00±0.00**	99.96±0.12	**100.00±0.00**	**100.00±0.00**	99.80±0.42
	Prec%	96.21±0.98	**96.60±0.69**	96.30±0.67	**100.00±0.00**	**100.00±0.00**	99.87±0.41	**100.00±0.00**	**100.00±0.00**	99.77±0.50
	F1	0.95±0.00	**0.96±0.00**	0.96±0.01	**1.00±0.00**	**1.00±0.00**	**1.00±0.00**	**1.00±0.00**	**1.00±0.00**	**1.00±0.00**
	Acc%	96.19±0.36	96.94±0.31	**97.04±0.35**	**100.00±0.00**	**100.00±0.00**	99.97±0.09	**100.00±0.00**	**100.00±0.00**	99.89±0.22
Full (LOOV)	**Sen%**	78.77	76.46	**79.09**	**100.00**	**100.00**	**100.00**	99.57	**100.00**	**100.00**
	Spec%	**88.06**	83.00	87.42	94.07	94.07	**100.00**	83.30	**84.24**	**84.24**
	Prec%	**81.94**	75.56	81.21	85.95	85.95	**100.00**	85.19	**85.95**	**85.95**
	F1	**0.80**	0.76	**0.80**	0.93	0.93	**1.00**	0.92	**0.93**	**0.93**
	Acc%	**84.28**	80.33	84.03	95.65	95.65	**100.00**	91.29	**91.98**	**91.98**
Delta (LOOV)	**Sen%**	69.79	71.06	**74.50**	**100.00**	99.57	99.68	**99.78**	97.19	99.46
	Spec%	73.85	69.76	**76.70**	94.03	**94.07**	**94.07**	83.82	**84.34**	84.24
	Prec%	64.72	61.77	**68.74**	85.87	85.90	**85.91**	85.61	85.69	**85.89**
	F1	0.67	0.66	**0.72**	**0.92**	**0.92**	**0.92**	**0.92**	0.91	**0.92**
	Acc%	72.19	70.29	**75.80**	**95.62**	95.53	95.56	91.66	90.65	**91.71**
Theta (LOOV)	**Sen%**	69.86	69.68	**81.61**	**99.68**	**99.68**	98.27	99.46	**99.68**	98.16
	Spec%	**83.98**	78.91	82.70	97.88	94.07	**100.00**	84.03	84.24	**84.24**
	Prec%	74.99	69.43	**76.43**	94.46	85.91	**100.00**	85.73	**85.91**	85.73
	F1	0.72	0.70	**0.79**	0.97	0.92	**0.99**	**0.92**	**0.92**	**0.92**
	Acc%	78.23	75.15	**82.25**	98.36	95.56	**99.53**	91.60	**91.82**	91.07
Alpha (LOOV)	**Sen%**	60.71	**70.80**	69.85	99.24	**100.00**	97.40	**99.03**	98.81	97.40
	Spec%	85.08	86.37	**85.13**	94.07	94.11	**84.24**	84.24	**84.97**	84.24
	Prec%	73.67	**78.12**	76.35	85.86	86.03	**85.63**	85.84	**86.38**	85.63
	F1	0.67	**0.74**	0.73	0.92	0.93	**0.91**	0.92	**0.92**	0.91
	Acc%	75.15	**80.03**	78.90	95.45	95.68	**98.44**	91.50	**91.76**	90.70
Beta (LOOV)	**Sen%**	72.96	72.15	**73.94**	**100.00**	**100.00**	99.78	**99.89**	99.24	99.68
	Spec%	86.81	89.31	**91.37**	93.95	93.99	**100.00**	**84.13**	83.61	83.93
	Prec%	79.18	82.27	**85.48**	85.71	85.79	**100.00**	**85.86**	85.38	85.67
	F1	0.76	0.77	**0.79**	0.92	0.92	**1.00**	**0.92**	**0.92**	**0.92**
	Acc%	81.17	82.32	**84.27**	95.56	95.59	**99.94**	**91.87**	91.29	91.66

99.90% for the unbalanced and balanced versions of dataset 2, respectively.

Similarly, for specificity, in dataset 1, the full band has obtained 99.15%, followed by beta (97.68%), theta (94.65%), alpha (91.96%), and delta (88.27%). For unbalanced dataset 2, those values are full (100%), beta (100%), theta (100%), alpha (99.96%) and delta (99.96%). For balanced dataset 2, those are full (100%), beta (100%), theta (100%), alpha (99.67%) and delta (100%).

For dataset 1, the full band's highest precision value is 98.75%, the beta band is 96.60%, the theta band is 92.02%, the alpha band is 87.76% and the delta band is 82.35%. For balanced dataset 2, all bands except alpha (99.70%) have achieved 100% precision values. For unbalanced dataset 2, full, beta, and theta have achieved 100% precision, while alpha has 99.91% and delta has 99.87%. The F1 score also shows the same pattern as the other parameters depicted for all the datasets.

On the other hand, in the case of LOOV, for dataset 1, the highest accuracy of 84.28% has been achieved using full band, followed by beta (84.27%), theta (82.25%), alpha (80.03%), and delta (75.80%). For unbalanced dataset 2, those values are 100% (full), 99.94% (beta), 99.53% (theta), 98.44% (alpha), and 95.62% (delta). For balanced dataset 2, those values are 91.98%, 91.87%, 91.82%, 91.76%, and 91.71% for full, beta, theta, alpha, and delta bands, respectively. Although the

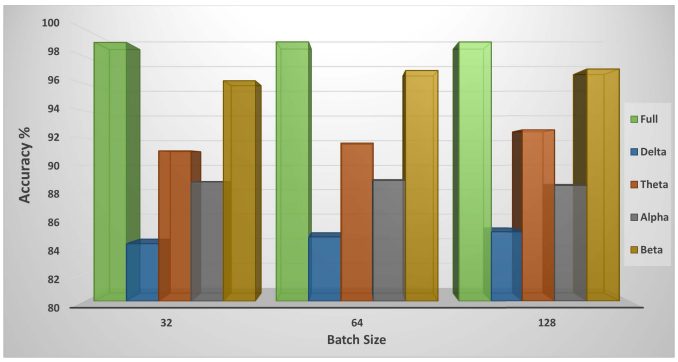

(a) Accuracy of dataset 1

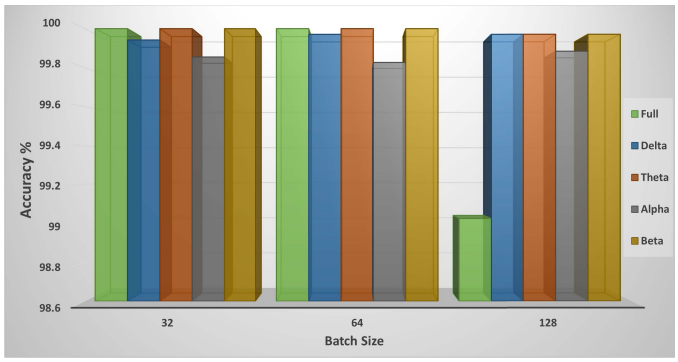

(b) Accuracy of dataset 2

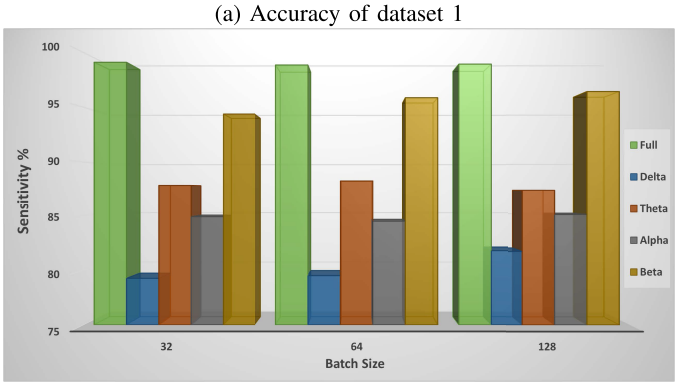

(c) Sensitivity of dataset 1

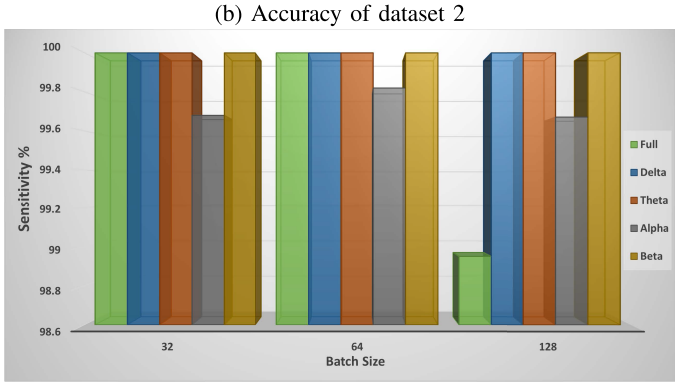

(d) Sensitivity of dataset 2

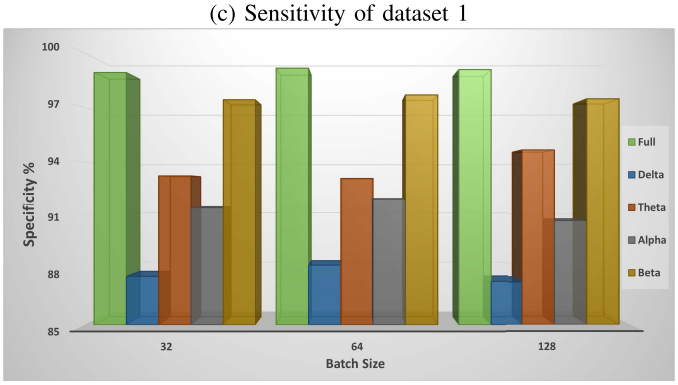

(e) Specificity of dataset 1

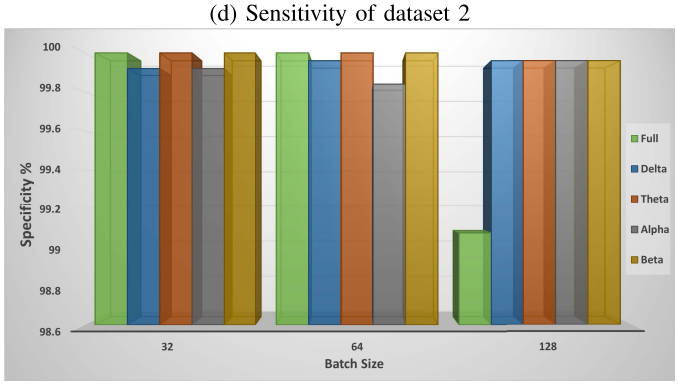

(f) Specificity of dataset 2

Fig. 3. Comparison of different evaluation parameters for the tested datasets for different frequency sub-bands in 10-fold CV. Figs. 3a, 3c, and 3e show the accuracy, sensitivity, and specificity for dataset 1. Figs. 3b,3d, and 3f show the accuracy, sensitivity, and specificity for the unbalanced dataset 2.

accuracy for LOOV is good, but a bit less comparatively 10-fold CV for dataset 1 and balanced version of dataset 2. This is because three subjects in dataset 1 and one subject in balanced dataset 2 have accuracy below 40%.

From the obtained result, we can see that for dataset 1, among the tested four frequency bands, the beta band has produced the best performance compared to other bands for both the 10-fold CV and LOOV approaches and is closer to the performance using the full band. The next best result is produced by the theta band, followed by the alpha and delta bands. For the unbalanced dataset 2, sub-band theta also produced the same result as the beta band in 10-fold CV, but for LOOV, it also follows the same trend as dataset 1. For the balanced dataset 2 in 10-fold CV, all sub-bands except alpha have produced the same classification accuracy, but for LOOV, beta has given the best performance, followed by theta, and then alpha and delta.

To further compare the change in values for different evaluation parameters for different sub-bands, we have plotted those in the graphs as shown in Fig. 3. These graphs show the changes in the evaluation parameters for different frequency bands with the change in training batch size. From Figs. 3a, 3c, and 3e, we can see there are clear differences in performance among the four tested sub-bands. On the other hand, for unbalanced dataset 2, performance values have not changed that much as for dataset 1, but the performance has dropped a bit for sub-bands delta and alpha, similar to dataset 1. This is maybe due to the smaller size of dataset 2, as the dataset has a small amount of data in it.

Finally, to further compare the results, we have plotted the ROC curve for the best results obtained for dataset 1 and unbalanced dataset 2 in a 10-fold CV and given it in Fig. 4.

From Fig. 4b, we can see that, for unbalanced dataset 2, like other evaluation parameters, the ROC curve for different

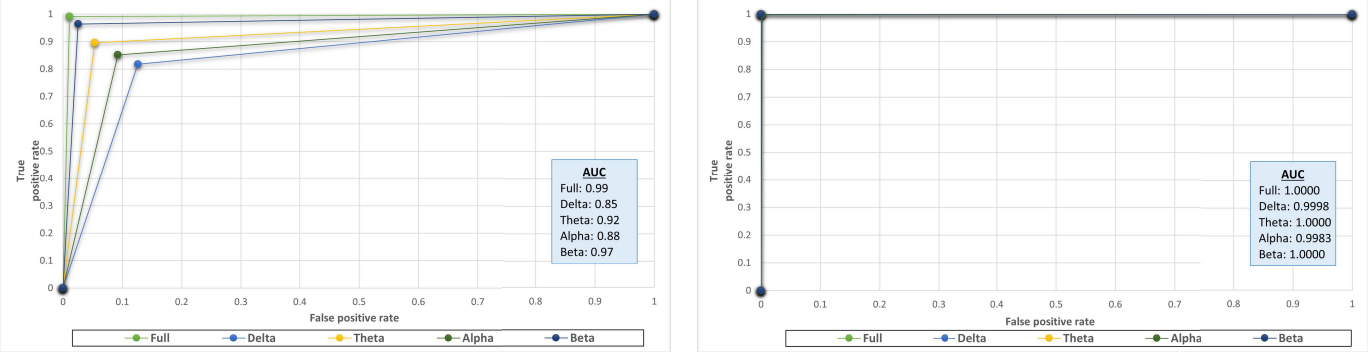

(a) Dataset 1 (b) Dataset 2

Fig. 4. Comparison of the ROC curves for the tested datasets for different frequency sub-bands. Fig. a and b show the ROC curve for datasets 1 and 2, respectively.

TABLE III
COMPARISON WITH THE EXISTING STUDIES OF MCI CLASSIFICATION USING DATASET 1

Study	Method	Validation	Accuracy	Sensitivity	Specificity
[16]	Spectral features with NF-*k*NN	Not given	88.89%	100.00%	83.33%
[18]	Spectral-temporal based features with SVM	Not given	96.94%	96.89%	96.99%
[1]	AR and PE based features with ELM	Subject-wise 10-fold	98.78%	98.32%	99.66%
[3]	GRU	5-fold	96.91%	97.95%	96.16%
[20]	LSTM	5-fold	96.41%	96.55%	95.95%
This study	Spectrogram image and CNN	10-fold	**99.03%**	98.87%	99.15%

frequency sub-bands overlaps with the curve generated using the full frequency band of the EEG signal. Also, the AUC values are 1 for the full, theta, and beta bands and close to 1 for the other two bands. On the other hand, for dataset 1, as given in Fig. 4a, the ROC curve of the full frequency band is closer to the (0, 1) point and the AUC is 0.99, which indicates that the spectrogram image generated using the 0.5-32 Hz bandwidth with the used CNN model is a good framework for MCI detection. Moreover, from the tested frequency sub-bands, the curve and AUC (0.97) of the beta (16-32 Hz) sub-band are much closer to the curve and AUC (0.99) of the full band curve, followed by the curve and AUC (0.92) of theta (4-8 Hz) sub-band.

C. Discussion

This study introduces an MCI detection algorithm based on spectrogram images and CNN classification techniques. We have tried to identify the important frequency sub-bands in EEG signals that significantly influence our proposed framework. Our study encompasses a bandwidth of 0.5 Hz to 32 Hz, which is recognized as containing essential features for MCI detection [18]. Spectrogram images are generated from this full signal band, and for sub-band analysis, we divide it into four segments: delta, theta, alpha, and beta. Delta waves are associated with deep sleep, unconsciousness, and some pathological conditions like encephalopathies or brain injuries [31]. Theta waves appear during relaxation, drowsiness, and sleep phases and play a role in cognitive and memory processes [21]. Alpha waves are prominent during relaxed wakefulness with closed eyes but diminish during cognitive activity, making them relevant in studies of concentration, relaxation, and meditation [21]. Beta waves are linked to active consciousness, cognitive processing, and attentiveness and can be associated with motor abilities and certain clinical disorders [21].

Certain frequency sub-bands of the EEG signal have been examined for their possible importance in the context of MCI detection. While there is still much to learn in this area of study, some research has emphasized certain frequency bands that may include vital information for MCI identification. Theta (4-8 Hz) is a frequently researched frequency range that has been linked to cognitive functions including memory recall and encoding [32], [33]. In contrast to HC, those with MCI have been found to exhibit changes in theta power and connection [32], [33]. Memory problems and cognitive decline have also been related to decreased theta activity [34].

Patients with MCI show anomalies in alpha power and coherence, particularly in the back of the brain, possibly affecting attention and functional connections [35], [36]. Moreover, the role of higher-frequency bands like beta in MCI diagnosis has been explored. Abnormal beta activity is linked to cognitive impairment and may serve as a biomarker for MCI [32], [37]. Specifically, there may be a reduction in beta power or changes in the synchronization of beta oscillations in certain brain regions [32], [37].

In this study, we have also found similar results about important frequency bands in MCI detection. Here, we have found that beta is the most important band in MCI detection, producing the highest accuracy among the four sub-bands across all the datasets and in both types of CV. Following the beta band, the theta band has produced the second highest

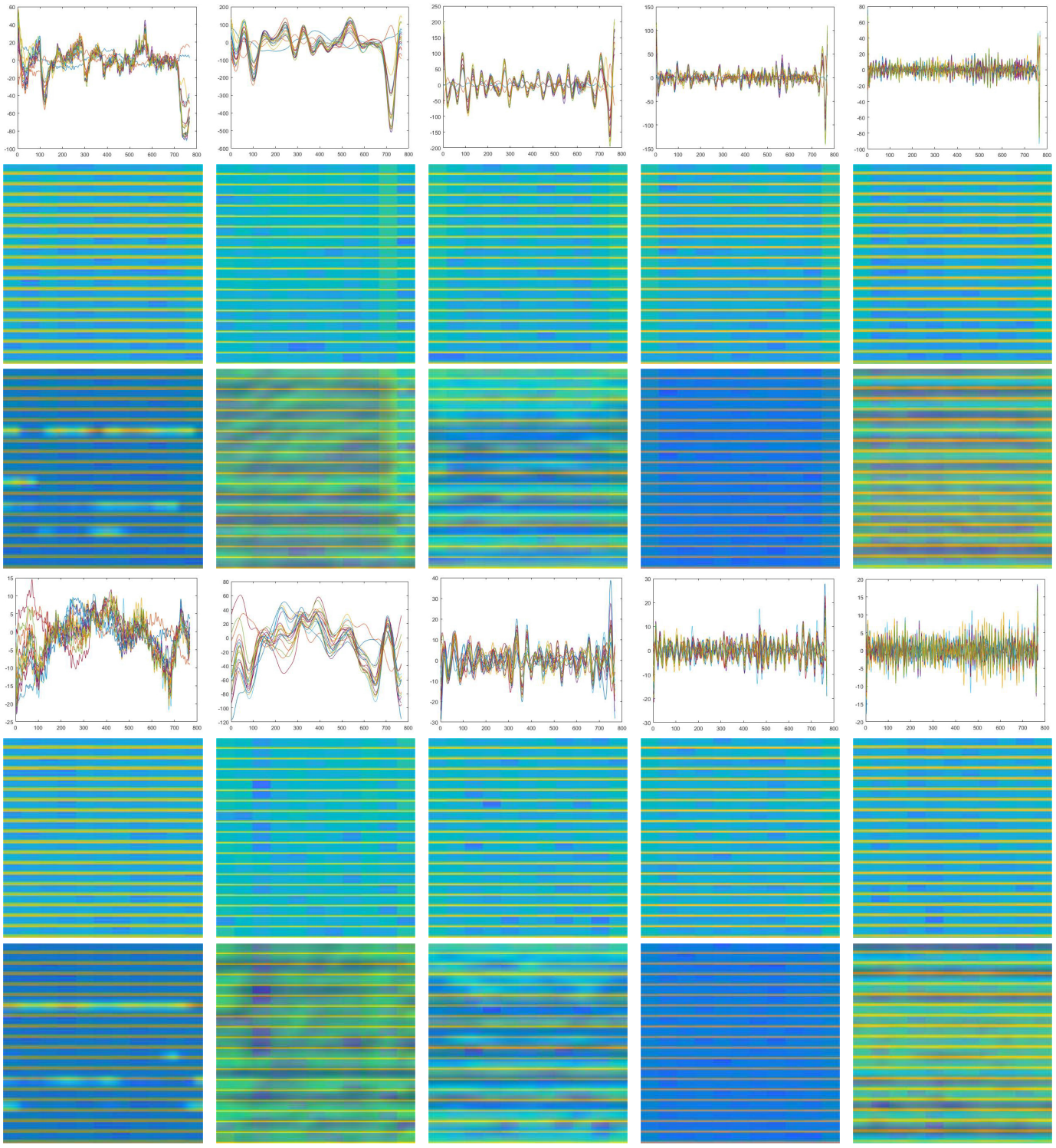

(a) Full (0.5-32 Hz) (b) Delta (0.5-4 Hz) (c) Theta (4-8 Hz) (d) Alpha (8-16 Hz) (e) Beta (16-32 Hz)

Fig. 5. Simple signal and corresponding spectrogram images generated by the proposed framework for dataset 1. The first row presents the raw EEG data for the HC subject, and the second and third rows represent their corresponding spectrograms and GRAD-CAM images. The fourth row presents the EEG data of a MCI subject, and the fifth and sixth rows show their corresponding spectrograms and GRAD-CAM images.

classification performance, followed by the alpha and delta bands. Based on the results, the identified important frequency band aligns with prior research findings [32], [35], [36], [37]. Moreover, according to the research, beta and theta sub-bands exhibit changes in power, and since spectrogram image pixel intensity reflects signal power, these two sub-bands offer higher accuracy compared to others.

A sample signal with the full frequency band and the generated four sub-bands from dataset 1 and their corresponding spectrogram and Grad-CAM images are given in Fig. 5. From

Fig. 5, we can see that for full, beta, and theta frequency bands, there are some specific areas where the discriminating patterns are different in the HC and MCI groups (the dense red color position differs in the HC and MCI images). But for the delta and alpha bands, those GRAD-CAM images don't contain any areas with dense red color, which is why the classification performance of those two sub-bands is lower compared to the other sub-bands.

Finally, to compare our framework against existing state-of-the-art (SoA) research that utilized the same datasets, we've presented a comparative table (Table III) that includes results from both ours and the relevant SoA studies.

From Table III, we can see that our study achieved better accuracy than all other studies that have used this dataset. Since dataset 2 is a three-class dataset (HC vs. MCI vs. AD), all the studies done using this dataset are three-class classification work. No study has used the MCI and HC sub-parts to perform a two-class classification, which is why we cannot compare the result with any other work on that dataset.

Although our proposed framework has achieved higher classification accuracy and has detected significant frequency bands for MCI classification using EEG signals, the main drawback of this study is the dataset. Though we have used two EEG datasets, the population size and length of the recording of those datasets are limited.

IV. Conclusion

In this study, a spectrogram image with a CNN model-based framework is proposed to classify MCI from HC using EEG data. We have used the framework to find the important frequency sub-bands in the classification process. We have filtered the signal between 0.5 Hz and 32 Hz, then segmented and generated spectrogram images from those signal segments. We have also divided those signals into four sub-bands and used the same framework to perform classification using those sub-bands. The framework is evaluated using both 10-fold CV and LOOV techniques on two different datasets of MCI. We have also tested three different training batch sizes to observe the impact of the batch size on training the model.

Using the full bandwidth, we have achieved better accuracy than the existing studies. Moreover, among the extracted four sub-bands, we have found that the sub-band named beta has a high contribution to the classification of the MCI signal from HC data. The second-highest contributor is the alpha sub-band. So, the obtained results indicate that the major classification features for MCI detection reside in the frequency band of 0.5-32 Hz, or, to be more specific, in the bandwidth of 16-32 Hz, followed by 4-8 Hz. Finally, the findings show that this method can be used to categorize other neurological disorders and can also be used in other signal processing tasks.

References

[1] S. Siuly et al., "A new framework for automatic detection of patients with mild cognitive impairment using resting-state EEG signals," *IEEE Trans. Neural Syst. Rehabil. Eng.*, vol. 28, no. 9, pp. 1966–1976, Sep. 2020.

[2] *Mild Cognitive Impairment*, Dementia Australia, Sydney, NSW, Australia, Feb. 2023.

[3] A. M. Alvi, S. Siuly, H. Wang, K. Wang, and F. Whittaker, "A deep learning based framework for diagnosis of mild cognitive impairment," *Knowl.-Based Syst.*, vol. 248, Jul. 2022, Art. no. 108815.

[4] P. M. Rodrigues, B. C. Bispo, C. Garrett, D. Alves, J. P. Teixeira, and D. Freitas, "Lacsogram: A new EEG tool to diagnose Alzheimer's disease," *IEEE J. Biomed. Health Informat.*, vol. 25, no. 9, pp. 3384–3395, Sep. 2021.

[5] Z. You et al., "Alzheimer's disease classification with a cascade neural network," *Frontiers Public Health*, vol. 8, Nov. 2020, Art. no. 584387.

[6] *Provisional Mortality Statistics*, Australian Bureau of Statistics, Canberra, ACT, Australia, May 2023.

[7] *The top 10 Causes of Death*, WHO, Geneva, Switzerland, May 2023.

[8] P. Durongbhan et al., "A dementia classification framework using frequency and time-frequency features based on EEG signals," *IEEE Trans. Neural Syst. Rehabil. Eng.*, vol. 27, no. 5, pp. 826–835, May 2019.

[9] M. N. A. Tawhid, S. Siuly, and H. Wang, "Diagnosis of autism spectrum disorder from EEG using a time–frequency spectrogram image-based approach," *Electron. Lett.*, vol. 56, no. 25, pp. 1372–1375, Dec. 2020.

[10] M. Tawhid, N. Ahad, S. Siuly, K. Wang, and H. Wang, "Data mining based artificial intelligent technique for identifying abnormalities from brain signal data," in *Proc. Int. Conf. Web Inf. Syst. Eng.* Cham, Switzerland: Springer, 2021, pp. 198–206.

[11] M. N. A. Tawhid, S. Siuly, H. Wang, F. Whittaker, K. Wang, and Y. Zhang, "A spectrogram image based intelligent technique for automatic detection of autism spectrum disorder from EEG," *PLoS ONE*, vol. 16, no. 6, Jun. 2021, Art. no. e0253094.

[12] M. Tawhid, N. Ahad, S. Siuly, K. Wang, and H. Wang, "Brain data mining framework involving entropy topography and deep learning," in *Proc. Australas. Database Conf.* Cham, Switzerland: Springer, 2022, pp. 161–168.

[13] M. N. A. Tawhid, S. Siuly, and T. Li, "A convolutional long short-term memory-based neural network for epilepsy detection from EEG," *IEEE Trans. Instrum. Meas.*, vol. 71, pp. 1–11, 2022.

[14] M. N. A. Tawhid, S. Siuly, K. Wang, and H. Wang, "Textural feature based intelligent approach for neurological abnormality detection from brain signal data," *PLoS ONE*, vol. 17, no. 11, Nov. 2022, Art. no. e0277555.

[15] M. N. A. Tawhid, S. Siuly, K. Wang, and H. Wang, "Automatic and efficient framework for identifying multiple neurological disorders from EEG signals," *IEEE Trans. Technol. Soc.*, vol. 4, no. 1, pp. 76–86, Mar. 2023.

[16] H. Rabbani, M. Kashefpoor, and M. Barekatain, "Automatic diagnosis of mild cognitive impairment using electroencephalogram spectral features," *J. Med. Signals Sensors*, vol. 6, no. 1, p. 25, 2016.

[17] S. Khatun, B. I. Morshed, and G. M. Bidelman, "A single-channel EEG-based approach to detect mild cognitive impairment via speech-evoked brain responses," *IEEE Trans. Neural Syst. Rehabil. Eng.*, vol. 27, no. 5, pp. 1063–1070, May 2019.

[18] J. Yin, J. Cao, S. Siuly, and H. Wang, "An integrated MCI detection framework based on spectral-temporal analysis," *Int. J. Autom. Comput.*, vol. 16, no. 6, pp. 786–799, Dec. 2019.

[19] N. Sharma, M. H. Kolekar, K. Jha, and Y. Kumar, "EEG and cognitive biomarkers based mild cognitive impairment diagnosis," *IRBM*, vol. 40, no. 2, pp. 113–121, Mar. 2019.

[20] A. M. Alvi, S. Siuly, and H. Wang, "A long short-term memory based framework for early detection of mild cognitive impairment from EEG signals," *IEEE Trans. Emerg. Topics Comput. Intell.*, vol. 7, no. 2, pp. 375–388, Apr. 2023.

[21] W. Klimesch, "EEG alpha and theta oscillations reflect cognitive and memory performance: A review and analysis," *Brain Res. Rev.*, vol. 29, nos. 2–3, pp. 169–195, Apr. 1999.

[22] Ö. F. Alçin, S. Siuly, V. Bajaj, Y. Guo, A. Şengür, and Y. Zhang, "Multi-category EEG signal classification developing time-frequency texture features based Fisher vector encoding method," *Neurocomputing*, vol. 218, pp. 251–258, Dec. 2016.

[23] M. Li, X. Sun, W. Chen, Y. Jiang, and T. Zhang, "Classification epileptic seizures in EEG using time-frequency image and block texture features," *IEEE Access*, vol. 8, pp. 9770–9781, 2020.

[24] L. Yuan and J. Cao, "Patients' EEG data analysis via spectrogram image with a convolution neural network," in *Proc. Int. Conf. Intell. Decis. Technol.* Cham, Switzerland: Springer, 2017, pp. 13–21.

[25] Z. Aslan and M. Akin, "Automatic detection of schizophrenia by applying deep learning over spectrogram images of EEG signals," *Traitement du Signal*, vol. 37, no. 2, pp. 235–244, 2020.

[26] M. Cejnek, O. Vysata, M. Valis, and I. Bukovsky, "Novelty detection-based approach for Alzheimer's disease and mild cognitive impairment diagnosis from EEG," *Med. Biol. Eng. Comput.*, vol. 59, nos. 11–12, pp. 2287–2296, Nov. 2021.

[27] M. J. Rivera, M. A. Teruel, A. Maté, and J. Trujillo, "Diagnosis and prognosis of mental disorders by means of EEG and deep learning: A systematic mapping study," *Artif. Intell. Rev.*, vol. 55, no. 2, pp. 1209–1251, Feb. 2022.

[28] H.-C. Shin et al., "Deep convolutional neural networks for computer-aided detection: CNN architectures, dataset characteristics and transfer learning," *IEEE Trans. Med. Imag.*, vol. 35, no. 5, pp. 1285–1298, May 2016.

[29] S. Siuly, S. K. Khare, V. Bajaj, H. Wang, and Y. Zhang, "A computerized method for automatic detection of schizophrenia using EEG signals," *IEEE Trans. Neural Syst. Rehabil. Eng.*, vol. 28, no. 11, pp. 2390–2400, Nov. 2020.

[30] Siuly, X. Yin, S. Hadjiloucas, and Y. Zhang, "Classification of THz pulse signals using two-dimensional cross-correlation feature extraction and non-linear classifiers," *Comput. Methods Programs Biomed.*, vol. 127, pp. 64–82, Apr. 2016.

[31] M. Steriade, A. Nunez, and F. Amzica, "A novel slow (< 1 Hz) oscillation of neocortical neurons in vivo: Depolarizing and hyperpolarizing components," *J. Neurosci.*, vol. 13, no. 8, pp. 3252–3265, Aug. 1993.

[32] J. P. Amezquita-Sanchez, N. Mammone, F. C. Morabito, S. Marino, and H. Adeli, "A novel methodology for automated differential diagnosis of mild cognitive impairment and the Alzheimer's disease using EEG signals," *J. Neurosci. Methods*, vol. 322, pp. 88–95, Jul. 2019.

[33] S.-S. Poil, W. de Haan, W. M. van der Flier, H. D. Mansvelder, P. Scheltens, and K. Linkenkaer-Hansen, "Integrative EEG biomarkers predict progression to Alzheimer's disease at the MCI stage," *Frontiers Aging Neurosci.*, vol. 5, p. 58, Oct. 2013.

[34] J. P. Trammell, P. G. MacRae, G. Davis, D. Bergstedt, and A. E. Anderson, "The relationship of cognitive performance and the theta-alpha power ratio is age-dependent: An EEG study of short term memory and reasoning during task and resting-state in healthy young and old adults," *Frontiers Aging Neurosci.*, vol. 9, p. 364, Nov. 2017.

[35] C. J. Stam et al., "Magnetoencephalographic evaluation of resting-state functional connectivity in Alzheimer's disease," *NeuroImage*, vol. 32, no. 3, pp. 1335–1344, Sep. 2006.

[36] D. Moretti, "Individual analysis of EEG frequency and band power in mild Alzheimer's disease," *Clin. Neurophysiol.*, vol. 115, no. 2, pp. 299–308, Feb. 2004.

[37] E. Başar et al., "What does the broken brain say to the neuroscientist? Oscillations and connectivity in schizophrenia, Alzheimer's disease, and bipolar disorder," *Int. J. Psychophysiol.*, vol. 103, pp. 135–148, May 2016.

[38] R. R. Selvaraju, M. Cogswell, A. Das, R. Vedantam, D. Parikh, and D. Batra, "Grad-CAM: Visual explanations from deep networks via gradient-based localization," in *Proc. IEEE Int. Conf. Comput. Vis. (ICCV)*, Oct. 2017, pp. 618–626.

[39] I. Goodfellow et al., "Convolutional networks," in *Deep Learning*. Cambridge, MA, USA: MIT Press, 2016, pp. 330–372.